



Facile one-pot controlled synthesis of Sn and C codoped single crystal TiO₂ nanowire arrays for highly efficient photoelectrochemical water splitting



Belete Asefa Aragaw^a, Chun-Jern Pan^a, Wei-Nien Su^b, Hung-Ming Chen^a, John Rick^a, Bing-Joe Hwang^{a,c,*}

^a NanoElectrochemistry Laboratory, Department of Chemical Engineering, National Taiwan University of Science and Technology, Taipei 106, Taiwan

^b NanoElectrochemistry Laboratory, Graduate Institute of Applied Science and Technology, National Taiwan University of Science and Technology, Taipei 106, Taiwan

^c National Synchrotron Radiation Research Center, Hsinchu 30076, Taiwan

ARTICLE INFO

Article history:

Received 2 June 2014

Received in revised form 13 August 2014

Accepted 19 August 2014

Available online 26 August 2014

Keywords:

TiO₂

PEC

Photocatalysis

Water splitting

Codoping

ABSTRACT

Here we report a (Sn, C) cation–anion codoped single crystal TiO₂ nanowire (NW) arrays as a highly efficient solar water splitting photoelectrode, able to be fabricated using a facile one pot hydrothermal synthesis method. The synergetic effects of codoping on the photoelectrochemical activity of the photoanode were investigated and compared to undoped and monodoped photoelectrodes. The (Sn, C) codoped TiO₂ NW photoanode generated the highest saturated photocurrent density i.e. 2.8 mA/cm² at 1.23 V vs RHE while yielding a maximum solar energy conversion efficiency of 1.32% at a potential of 0.55 V vs RHE – representing 60%, 94%, and 100% efficiency improvements compared to undoped, Sn doped, and C doped TiO₂ NW respectively at same potential. This improvement is attributed to the synergetic effects of Sn and C codopants to lower recombination and enhance life time of photogenerated charge-separated carriers on the surface states that lead to efficient hole transfer at the photoelectrode/electrolyte interface. In addition, an increased charge carrier density and conductivity (as evidenced from electrochemical impedance spectroscopy) and the enhanced incorporation of dopants in the codoped system, compared to monodoped system as quantified by XPS, highlights the importance of codoping. The nanomaterial was characterized by XRD, TEM, SEM and Raman UV–vis measurements. This study will guide improvements in the efficiency of TiO₂ for PEC water splitting using optimized codopant pairs.

© 2014 Elsevier B.V. All rights reserved.

1. Introduction

The increasing demand for sustainable, carbon-free energy production is driving the development of solar energy conversion and storage technologies. Photoelectrochemical (PEC) water splitting, that captures solar energy and stores it in the chemical bond of H₂ that can be used in several applications, is a promising way to address energy and environmental issues. Many semiconductor metal oxides have been examined to develop photoelectrodes that can harvest sunlight effectively and catalyze the photoelectrolysis of water into molecular hydrogen and oxygen. Different methods

have been employed to improve the efficiency of semiconductor materials for photoelectrochemical water splitting. Some of these include anchoring a non-noble metal [1] or noble metal [2] water oxidation catalyst, activating wide band gap semiconductors in the visible light region by ion implantation and doping [3,4]. Heterogeneous metal oxide semiconductor photocatalysts, such as TiO₂, WO₃, Fe₂O₃, and ZnO, are inherently photoactive and can perform water splitting, while retaining excellent chemical stability in aqueous solution. The solar-to-hydrogen (STH) conversion efficiencies for these materials are still rather low, compared to theoretically expected values, because of their intrinsic limitations. For TiO₂ and ZnO for instance, their relatively large band-gap (>3.0 eV) limits visible light absorption and thereby STH conversion efficiency. In comparison, α-Fe₂O₃ is a semiconductor metal oxide with an indirect band-gap of 2.1 eV, which is encouraging for visible light absorption. Yet, its efficiency has been harshly restricted by its intrinsic material properties such as its short excited state lifetime

* Corresponding author at: NanoElectrochemistry Laboratory, Department of Chemical Engineering, National Taiwan University of Science and Technology, Taipei 106, Taiwan. Tel.: +886 2 2736624; fax: +886 2 27376644.

E-mail address: bjh@mail.ntust.edu.tw (B.-J. Hwang).

(~10 ps), short hole diffusion distance (2–4 nm) and low-lying conduction band (~0.3 V below the water reduction potential) [5–7]. TiO_2 is the best known photocatalyst for overall water splitting into H_2 and O_2 – unlike WO_3 and $\alpha\text{-Fe}_2\text{O}_3$, which are used only for water oxidation, due to their low lying conduction band positions.

In this regard, TiO_2 has been one of the most investigated photoanode materials since the first report of solar driven PEC energy conversion [8] and has remained as one of the most promising candidates due to its high photocatalytic activity, appropriate band edge positions for overall water splitting, strong optical absorption, chemical stability, photo-corrosion resistance, non-toxicity, and low cost [9–14]. TiO_2 materials with highly reactive crystal facets e.g. (1 1 1) and (0 0 1) surfaces [15,16] have been synthesized for photocatalytic water splitting and organic dye degradation. Much research has been devoted to addressing the large band gap of TiO_2 (3.0 eV for rutile) by coupling it with small band gap semiconductors [17]. Cation and/or anion doping (or alloying) [18,19], post growth hydrogen annealing [20], or by surface sensitization with organic dyes to improve the photocatalytic efficiency. Due to high intrinsic trap densities in TiO_2 , it has a high charge carrier recombination rate, which is worsened by monodoping with cations or anions [13]. Heterostructuring the TiO_2 by codoping with two or more dopants is reported to achieve significant synergistic effects compared to their single ion doped or undoped TiO_2 counterparts, due to the strong interaction between these codopants within the TiO_2 matrix that alters the charge carrier transfer-recombination dynamics [21]. Codoping results in a much better effect on band gap narrowing due to strong interactions between the dopant metal and non-metal ions resulting in strong hybridization that gives rise to a fully occupied band above the top of the valence band edge and an empty band below the bottom of the conduction band [22]. Much theoretical work suggests that codoping TiO_2 improves light absorption, material quality, and the solubility limit of dopants [23–26]. A one-dimensional TiO_2 NW [27] structure has received much attention for PEC water splitting due to its large surface area, fast charge transport, and short diffusion distance for the photogenerated carriers [28,29]. Tin doping of TiO_2 [30,31] is essential as SnO_2 and TiO_2 have a low lattice mismatch that gives good structural compatibility and material stability. The incorporation of Sn or SnO_2 into TiO_2 by doping [31–33], to form core-shell structures [34], and heterostructure composites [30,35] has been shown to enhance photocatalytic activity. Doping TiO_2 with carbon is considered to be a promising way to improve the photocatalytic properties of TiO_2 photoanode for water splitting [36,37] and for pollutant decomposition [38]. Theoretically, compared to other N-cation codoped systems, C-cation systems exhibit greater band gap narrowing due to deeper C acceptor energy levels and much stronger interactions between C and the cations [22].

The advantages of TiO_2 , e.g. its high photocatalytic activity, well-positioned band edges, strong optical absorption, chemical stability, photo corrosion resistance, non-toxicity, and its low cost need to be balanced against its limited photon-to-hydrogen efficiency. This results from its large band gap and the rapid recombination of photogenerated electrons and holes as a result of the high intrinsic trap density. We believe a metal/nonmetal codoped TiO_2 photoanode material treated with hydrogen can result in an enhanced PEC performance for water splitting.

Only few reports feature TiO_2 codoped with cations and anions, prepared by sol–gel [39] and hydrolysis precipitation methods [40], for photocatalytic activity with degradation of organic dyes. As yet, no report has demonstrated experimental work applying codoped TiO_2 NW to PEC water splitting – except for one that used sequential ex situ flame doping at 1100 °C [41].

In this study we fabricated a single crystal TiO_2 NW array photoanode codoped with Sn and C in a facile one pot hydrothermal

synthesis method and investigated its PEC solar water splitting performance. Our material generated a saturated photocurrent density greater than the best current literature values under standard conditions [31,41]. The Sn only doped, C only doped and undoped TiO_2 NW arrays were also synthesized under the same reaction conditions for photoactivity comparisons with the codoped TiO_2 NW. All the samples were annealed in air at 450 °C for 2 h to increase crystallinity and further annealed in reducing gas (50% H_2 + 50% Ar) for an additional 60 min at 450 °C. A complete material characterization and PEC water splitting performance were performed. The amounts of Sn and C dopants were controlled by the concentrations of SnCl_4 and the glucose precursor reactant mixtures respectively. The pristine TiO_2 NW photoanode generated a saturated photocurrent density of 2.25 mA/cm² at 1.23 V vs RHE which is in agreement with literature values [20]. A maximum solar-to-fuel (STH) efficiency of 1.32% was achieved for the (Sn, C) codoped TiO_2 NW, which represents 60%, 94%, and 100% efficiency improvements compared to undoped, Sn doped, and C doped TiO_2 NW respectively at the same potential.

2. Experimental

2.1. Materials and synthesis

Titanium (IV) n-butoxide (99%), tin (IV) chloride (99%, anhydrous), $\alpha\text{-D (+)-glucose}$ (99%, anhydrous) all from ACROS ORGANICS and HCl (37%) were used for the photoelectrode synthesis. Fluorine-doped tin oxide (FTO, 15 Ω) coated glass substrate was cleaned prior to use by sonicating with a 1:1:1 mixture of deionized water, acetone and 2-propanol prior to oven drying. Pristine TiO_2 , Sn-doped, C-doped and (Sn, C)-codoped TiO_2 NW arrays were grown on FTO using a previously reported hydrothermal method [27]. In a typical synthesis, 15 ml of deionized water and 13 ml of concentrated hydrochloric acid were mixed in a 100 ml Teflon-bomb containing FTO substrate with conducting side facing up. $\text{Ti (O}i\text{Bu)}_4$ solution (250 μl) was added into this mixture. Selected amounts (0–1.44 ml) of SnCl_4 (0.1 M) and glucose (0–4.4 mg) as carbon dopant precursors were added into same reaction solution. The Teflon bomb containing all these components was sealed in a stainless steel autoclave. The mixture was kept in an oven at 150 °C for 12 h after which the material grown on FTO was rinsed in deionized water. Next, the sample was annealed at 450 °C for 2 h in a furnace followed by treating it under 50% H_2 + Ar gas in a tube furnace at 450 °C for 1 h.

2.2. Characterization

X-ray diffraction measurements were performed on a D2 phaser XRD-300W diffractometer equipped with a Cu K α source operating at 30 kV and 10 mA. Scans were made from 20–80° 2 θ at a rate of 3° per minute. A dual-beam focused ion beam (FIB, FEI Quanta 3D FEG) equipped with scanning electron microscope (SEM) mode operated at an accelerating voltage of 30 kV was used to capture FIB images. For TEM sample preparation, thinning of the specimen was achieved through the process of sputtering with gallium ions using FIB technology. UV–vis diffused reflectance spectra of the samples were obtained using a JASCO (ISV-469) V 560 UV–Vis spectrometer. Micro-Raman spectroscopy was used to characterize the phase and defects using a 532 nm green laser. The TEM images and Energy-dispersive X-ray (EDX) mapping images were collected on a Philips/FEI Tecnai 20G2 S-Twin TEM apparatus. X-ray photoelectron spectra (XPS) (PHI, 1600S) were recorded at the National Synchrotron Radiation Research Centre (NSRRC), Taiwan with 24A XPS beam line station.

2.3. Photoelectrochemical measurement

The photoelectrochemical measurements were carried out in a 3-electrode system with Ag/AgCl as a reference electrode, Pt wire as counter electrode, and the TiO₂ NW photoanode as the working electrode. The light source used was a Hg–Xe lamp (Newport, 500W) coupled with a AM1.5G filter, calibrated to 100 mW/cm² (1 sun illumination) with silicon diode. The electrolyte used for PEC measurement was 1 M KOH(aq). Photocurrent density versus applied potential (*J*–*V*) and Photocurrent density versus time (*i*–*t*) were measured using an Autolab electrochemical work station with NOVA software with front side illumination. A potential window (–1 V to 0.4 V Vs Ag/AgCl) was scanned anodically during the *J*–*V* analysis. Mott–Schottky plots were performed at a frequency of 1 kHz in the dark.

3. Results and discussion

The morphology of the materials was observed using FIB imaging as in Fig. 1. Vertically oriented NWs of (Sn, C) codoped TiO₂ were uniformly grown on the FTO substrate (Fig. 1b–d). The entire surface of FTO is uniformly covered with the NW arrays. Fig. 1a also shows the morphology of pristine TiO₂. The undoped and monodoped TiO₂ showed the same morphology, confirming that the morphology of the NW is not changed after codoping TiO₂ with Sn and C. Unlike the pristine TiO₂ NW which is weak and less oriented, the codoped TiO₂ NW is strong and well-aligned even after being sputtered by a Ga⁺ ion beam during sample cutting for cross-sectional viewing. NW cross-sections show that NWs, not damaged by the focused ion beam during sample preparation, have diameters of 95–120 (average 107) nm and lengths from 2.55 to 2.8 μm (Fig. S1a). The TEM images shown in Fig. 2a and b show, with atomic resolution, the morphology of multiple and single NW's. High-resolution TEM (HRTEM) images in Fig. 2c revealed that the NW is single crystalline, which is confirmed by the corresponding fast-Fourier-transform (FFT) pattern that shows one set of points (Fig. 2c, inset). Lattice fringes of 0.325 and 0.292 nm were clearly observed, corresponding to the d-spacing values of the (1 1 0) and (0 0 1) planes of crystalline rutile TiO₂ [20,31,41]. The differential increase in spacing crystal planes observed is due to doping of larger atomic size Sn⁴⁺ (0.071 nm) and C^{4–} (0.260 nm) compared to Ti⁴⁺ (0.068 nm) and O^{2–} (0.140 nm) atoms [41]. This is in agreement with the lower angle shift observed in the X-ray diffraction pattern for the doped TiO₂ NW. Energy-dispersive X-ray spectrometer (EDX) mapping and scanning TEM images of the corresponding mapped area of the NW are shown in Fig. 2d. The mapping of a single NW for Sn dopant shows uniform distribution of Sn throughout the NW. However, the C signal suffered interference due to the carbon layered copper grid sample stage during mapping.

X-ray diffraction (XRD) spectroscopy was performed to determine the phase and crystal structure of the samples prepared. From Fig. 3a, the pristine TiO₂, Sn doped TiO₂, C doped TiO₂ and (Sn, C) codoped TiO₂ NWs are shown to have the same crystalline rutile phase. The diffraction peaks of the FTO substrate are plotted for comparison. The dopant can enter the TiO₂ lattice either interstitially or it can act as substitutional impurity. Substitution is governed by factors such as atomic size, crystal structure, electro negativity and relative valency. If these properties are closely matched, substitution is possible for all compositions [31]. The peak position of TiO₂ doped with Sn only, C only and codoped with (Sn, C) shifts to lower degree, corresponding to an increase in the lattice parameter, due to the larger ionic radius of Sn⁴⁺ (0.071 nm) and C^{4–} (0.260 nm) compared to Ti⁴⁺ (0.068 nm) and O^{2–} (0.140 nm) as well as the coulombic repulsion force between the ionic charges. This lattice fringe expansion phenomenon is also observed in HRTEM

images (Fig. 2c). These observations confirm the successful doping of the Sn and C atoms in TiO₂ matrix.

Fig. 3b shows the optical property of the material as studied by UV–vis diffuse reflectance measurements. The absorption edge for the (Sn, C) codoped TiO₂ NW was red-shifted compared to all other samples, thereby confirming the effectiveness of band gap narrowing by codoping. C doped TiO₂ NW has the next longest wave length onset absorption after the codoped sample. The absorption edges of pristine TiO₂ and Sn doped TiO₂ were at the lower wavelength side. The C-doped and pristine TiO₂ NW has higher absorption in the 420–800 nm region than codoped and Sn doped TiO₂. In case of (Sn, C) doped and Sn only doped TiO₂, the interaction of Sn⁴⁺ cation with Ti⁴⁺ can control the type and formation of defects during sample treatment in H₂ atmosphere. The higher absorption might be due to the increase in defects/oxygen vacancies formed during H₂ treatment acting as a color center [20,42]. Likewise, the increased peak intensity at about 230 cm^{–1} in Raman spectra (Fig. S3) for the pristine and C doped TiO₂ corresponded to a multi-photon process which is believed to be related to the increased defects after H₂ treatment [43,44]. The four Raman vibration modes observed are particular to the rutile phase of TiO₂, which further confirms the phase identification observed in XRD.

Fig. 3c shows the determination of the band gap of the TiO₂ NW by plotting $[\alpha E]^n$ ($n = 1/2$ for indirect band gap material) vs. energy ($h\nu$) from UV–vis measurements [45]. The line drawn at the linear portion of $[\alpha E]^{1/2}$ at $E = 0$ gives the value of band gap from the Tauc plot. The (Sn, C) codoped TiO₂ NW showed the lowest band gap compared to all other samples. This is in agreement with theoretical reports showing the importance of codoping TiO₂ with cations and anions to narrow its band gap [23–25]. Based on the band gap determined from UV–vis and the flat band potential determined from the Mott–Schottky plot (Fig. 6), a proposed electronic band structure for the materials is shown in Scheme 1.

The electronic properties of the (Sn, C) codoped TiO₂ NWs are affected by both the cation and anion. The Sn⁴⁺ state modulates the conduction band (containing the Ti 3d orbital) of TiO₂. Some donor states of Sn orbital will lie below the conduction edge of TiO₂. By doping anions e.g. C to the TiO₂ matrix, the acceptor states of C orbitals will form above the valence band edge of TiO₂. Hence, doping both a Sn cation and a C anion resulted in band gap narrowing as the conduction band was down-shifted by the Sn orbitals and the valence band up-shifted by the C orbitals. In addition, H₂ treatment of TiO₂ forms a defect (Ti³⁺ and oxygen vacancy) that forms a donor level below the conduction band of TiO₂ [20,44,46].

High-resolution XPS was used to confirm the presence and chemical states of Ti, Sn, C, and O in our samples as shown in Fig. 4. Ti 2p_{3/2} and 2p_{1/2} typical peaks of TiO₂ (Fig. 4a) were centered at 458.6 eV and 464.4 eV – these values being consistent with those in the literature [47]. In Sn only doped and (Sn, C) codoped TiO₂, a slight positive shift in binding energy was observed compared with the undoped TiO₂. This is attributed to the substitution of less electronegative Ti atoms by more electronegative Sn atoms that results in the shift of electron density from Ti to Sn. In case of C only doped TiO₂, there is no visible shift in the Ti2p binding energy. This suggests that C is interstitially doped in the TiO₂ matrix to form carbonate species. Fig. 4b shows the O 1s peak for all TiO₂ samples at 530.2 eV with a shoulder peak at 532 eV corresponding to lattice oxygen and surface hydroxyl oxygen atoms respectively [47]. A small positive shift of the lattice oxygen binding energy in Sn only doped and (Sn, C) codoped TiO₂ further confirms the substitution of Ti atoms with more electronegative Sn atoms. In case of C only doped TiO₂, there is no lattice oxygen peak shift observed which further confirms the interstitial doping of C. The deconvoluted O1s peak that revealed different types of oxygen atoms is shown in Fig. S4. In Fig. 4c, the Sn only doped and (Sn, C) codoped TiO₂ displayed two peaks in Sn 3d region at 486.2 eV and 494.6 eV, unlike

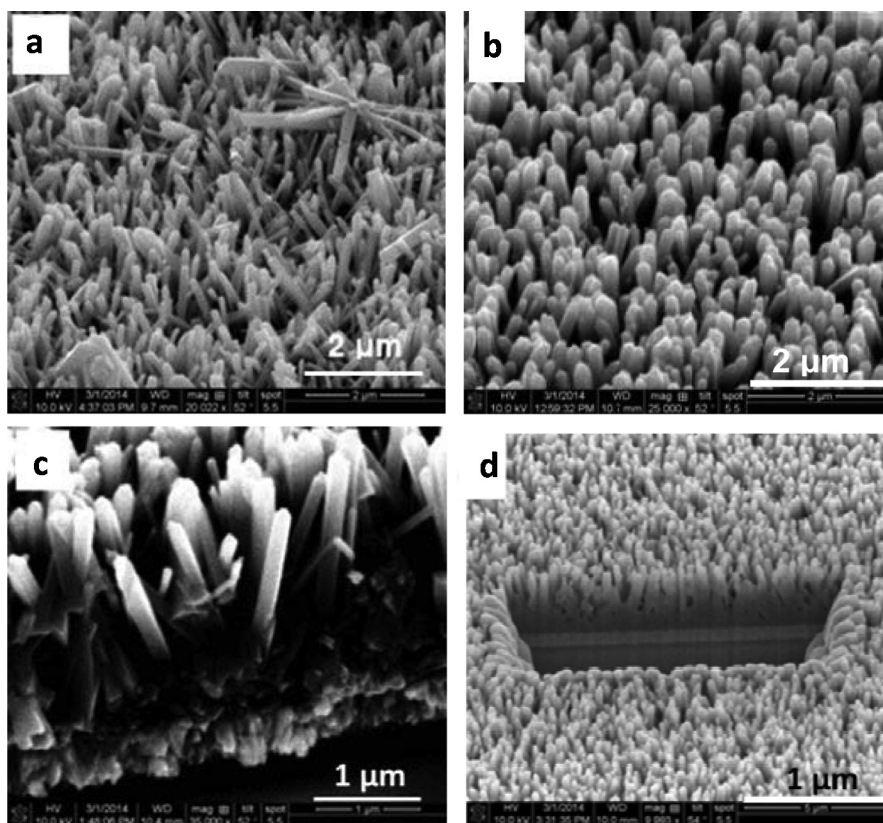


Fig. 1. Top surface view and edge view with 52° angle tilt FIB images of oriented rutile NW of undoped TiO₂ (a) and (Sn, C) codoped TiO₂ (b and c). Top surface view (a, b and d), edge view of sample broken by hand (c) and cut by FIB (d).

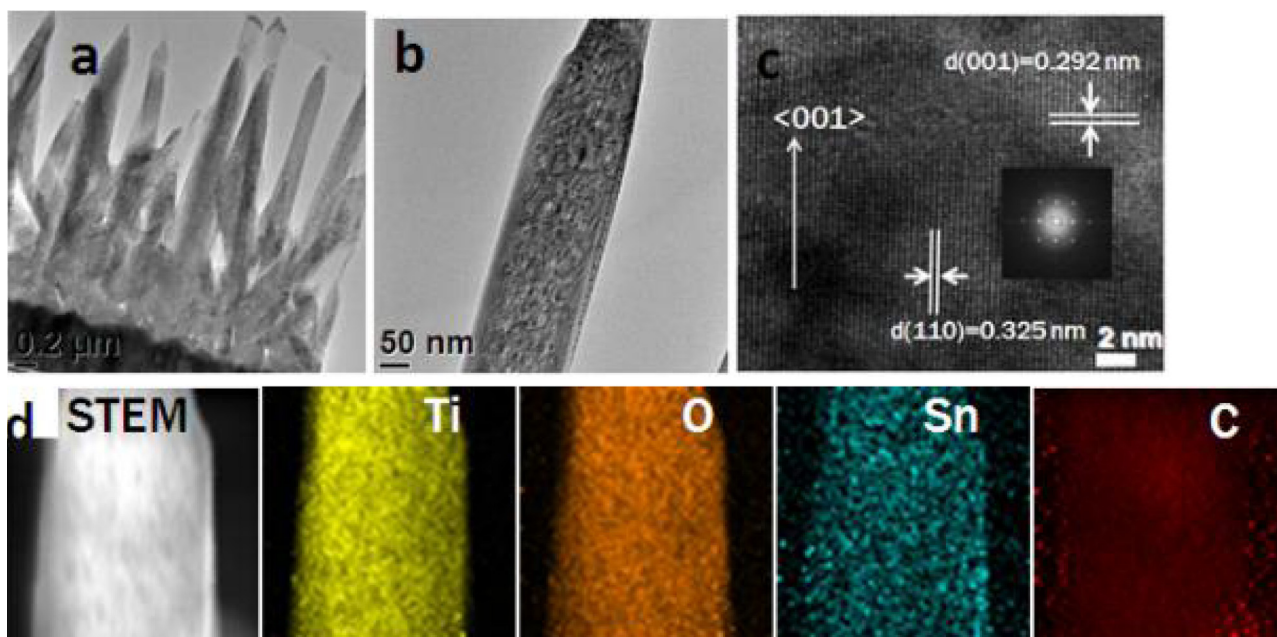


Fig. 2. TEM image of a typical (Sn, C) codoped TiO₂ NW. Multi and single NW (a and b). HR-TEM images and fast-Fourier-transform pattern (inset) showing single crystalline NW (c). TEM images of the scanned area and Energy-dispersive X-ray spectrometer mapping images for the elements Ti, O, Sn, and C (d).

the undoped TiO₂, corresponding to Sn 3d_{5/2} and 3d_{3/2}, which is consistent with literature values [33]. This phenomenon together with the positive peak shift in Ti 2p and the O1s of Sn-containing TiO₂, confirms the formation of the Ti–O–Sn structure, owing to the substitution of Ti by Sn. In addition, XPS quantitative analysis from peak area integration showed that the actual Sn/Ti ratio was

~3.2% for (Sn, C)/TiO₂ NW and 2.4% for Sn/TiO₂ NW. Interestingly the carbon codopant enhanced the incorporation of tin atoms. This is attributed to improved solubility limit of dopants due to codoping [22,24,25]. The C 1s spectra in Fig. 4d showed two peaks at 284.8 and 286.5 eV for both of the C-containing samples. The first value is an instrumental artifact related to elemental adventitious

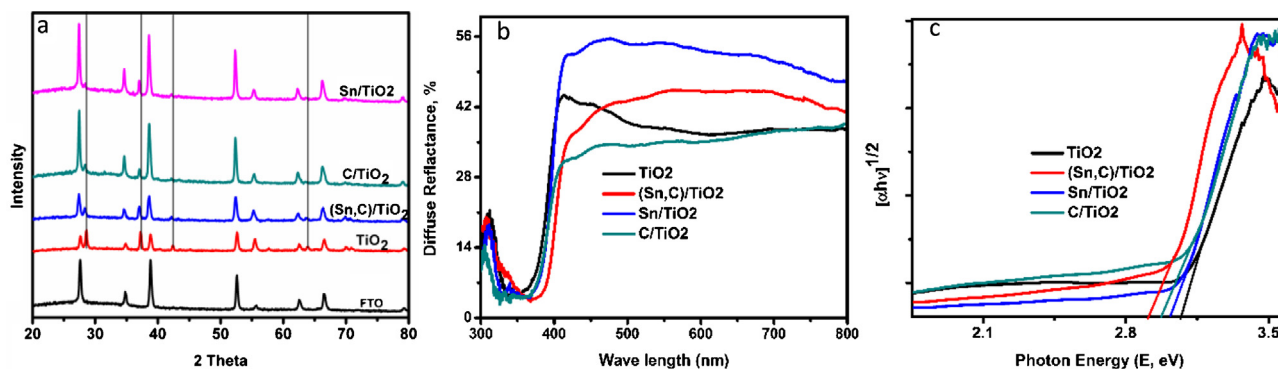
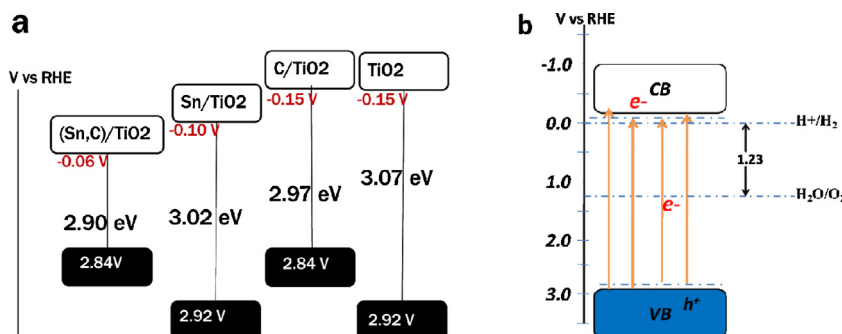


Fig. 3. Undoped, Sn doped, C doped, and (Sn, C) codoped TiO₂ NW on a FTO coated glass substrate: (a) XRD spectrum, (b) UV–vis diffuse reflectance spectra, and (c) Tauc plot for band gap estimation.



Scheme 1. Energy diagram of: (a) undoped, monodoped and codoped TiO₂ NW, (b) (Sn, C)/TiO₂ for with respect to H₂O/H₂ and O₂/H₂O potentials. Arrows highlight the possible electronic transitions between the different energy levels in (Sn, C) codoped TiO₂ NW.

carbon present in all XPS measurements [48,49]. The latter value has previously been related in the literature to interstitial carbonate dopants as well as oxidized carbon species adsorbed on the surface of the material [37,48,50,51]. Thus, it is worth noting that no obvious signal related to carbide (281.5 eV) was observed in our case, indicating that the amount of Ti-bonded carbon is very low, or that all the carbon is oxidized. Quantitative analysis showed that the actual C/O ratio is 7.4% for (Sn, C)/TiO₂ NW and 5.6% for C/TiO₂ NW. The amount of C in (Sn, C)/TiO₂ NW is higher than in C/TiO₂ NW even though the designed concentration is the same. This confirms the importance of codoping in enhancing the amount of dopants incorporated into the TiO₂ lattices.

To investigate the photocatalytic activity for solar energy driven water splitting, pristine, Sn doped, C doped TiO₂ and (Sn, C) codoped TiO₂ NW photoelectrodes were prepared. By varying the percentage of Sn and C dopants, the optimum amounts of the codopants that generate the best photoconversion efficiency was determined for both Sn and C co-incorporated into TiO₂ (Fig. S2). Optimum Sn and C percent codoped and monodoped TiO₂ NW photoanodes were separately characterized and investigated for photoelectrochemical performance. The optimal amount of Sn and C dopants was determined after measuring the PEC performance for the different (Sn, C) codoped TiO₂ samples. The Sn–C calculated atomic percent 5–5, 5–10, 5–15, 5–20, 10–5, 10–10, 15–5, 15–15, 20–5, and 20–20 codoped TiO₂ samples were synthesized and the corresponding photocurrent conversion efficiency was as given in Fig. S2. From the graph, we can see that the sample with same atomic percent of Sn and C generated higher photoconversion efficiency compared to the one with different percentages of Sn and C. Generally, the performance of the codoped TiO₂ increases with an increase in the amount of Sn and C and reaches maximum at 10% Sn and 10% C, and then starts to decrease with further increase in amount of Sn dopant. The same atomic percent of both dopants give

better performance compared to those with different percent of Sn and C. It might be due to best interaction of Sn and C when they exist in comparable amounts. The presence of one of the dopants in very high excess of the other dopants may lower the performance due to unbalanced interaction. When the amount of dopants is very low, it will be difficult to improve the property of the host material significantly. When a larger amount of dopants is incorporated, phase separation between TiO₂ and oxides of dopants will result interface scattering. This will negatively affect the PEC performance.

The photocurrent density, generated as a function of applied potential, is plotted in Fig. 5a and b. The photocurrent density of the (Sn, C) codoped TiO₂ NW shows an abrupt increase at the onset potential and saturates at significantly lower potential ~ 0.55 V vs. RHE unlike the photocurrent of undoped TiO₂ NW samples, which increased gradually with applied bias and reached saturation at a high applied bias. In the case of Sn only and C only doped TiO₂ NW, the increase in photocurrent density was much lower and saturated in a higher potential region. This shows that the recombination of photogenerated electrons and holes was higher compared to pristine and codoped TiO₂. On the other hand, the attainment of a saturated photocurrent with a very steep rise at lower potential indicates that the charge carrier transfer is efficient and surface recombination is suppressed [52]. In this regard, (Sn, C) codoped TiO₂ NW photoanode, compared to the pristine and monodoped TiO₂ NWs has lowest photogenerated charge carrier surface recombination in the low potential region. This can be explained by the synergetic effect of codopants that forms surface traps which can enhance the transient lifetime of charge carriers. The (Sn, C) codoped TiO₂ NW photoanode generated the highest saturated photocurrent density of 2.8 mA/cm² at 1.23 V vs RHE. The photocurrent densities, generated at 0.55 V vs RHE, that give maximal STH efficiencies are 2, 1.1, 0.59, and 0.46 mA/cm² for codoped, undoped, Sn doped, and C doped TiO₂ NW respectively. The photocurrent

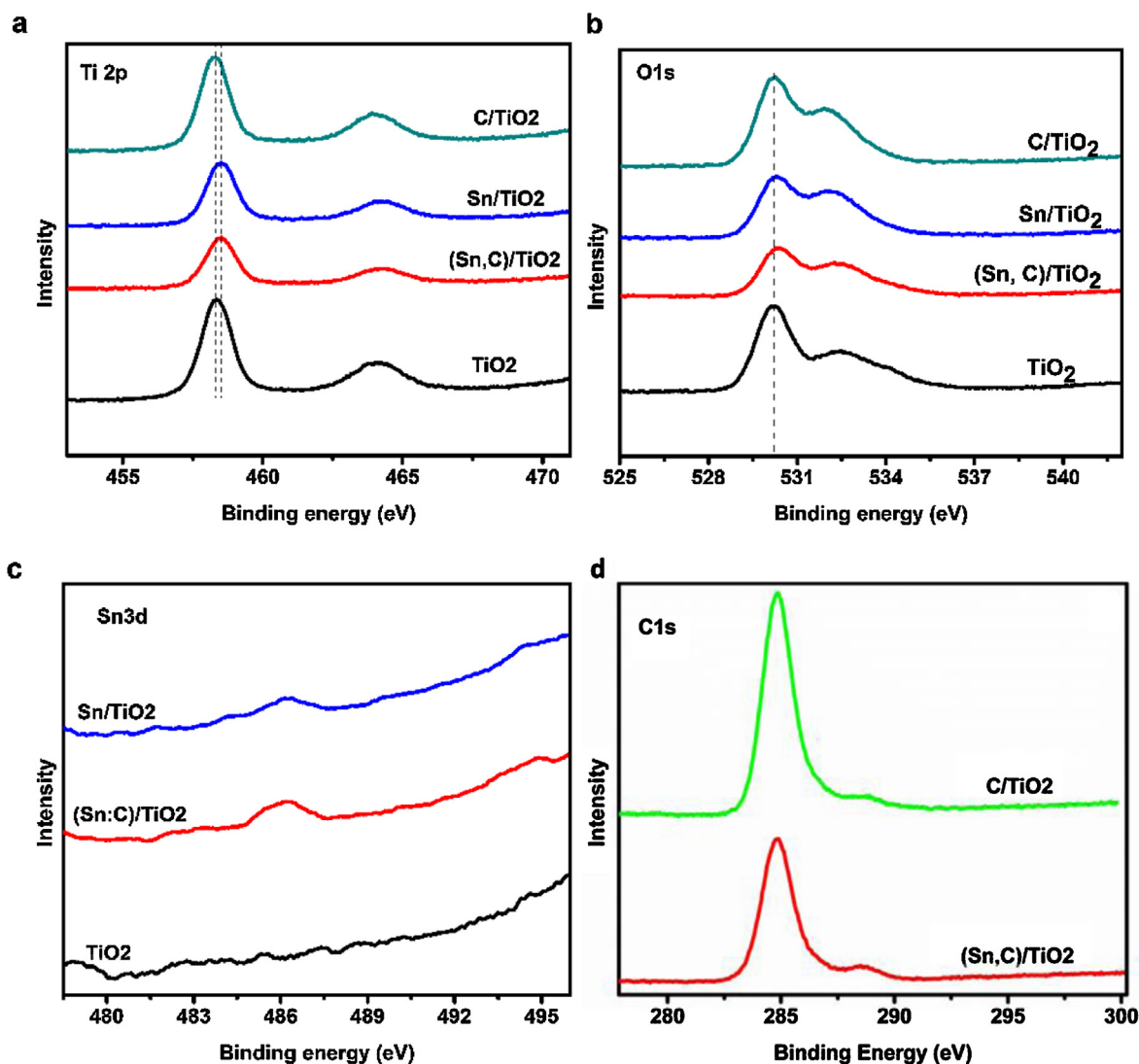


Fig. 4. XPS peaks of Ti2p, O1s, Sn3d, and C1s for undoped, monodoped and codoped TiO₂ NW.

generated by hydrogen treated undoped TiO₂ NW is in agreement with literature values [20].

It is desirable to use lower energy photocurrent onsets and saturation potentials to achieve the maximum photocurrent density, since the photoconversion efficiency of the material depends on the applied bias used. The photoconversion efficiency which is similar to solar-to-hydrogen efficiency (η) of the NW photoanode can be calculated from the J – V using the following equation [53].

$$\eta = \frac{J_p(1.23 - V_{pp})}{I_0} \quad (1)$$

where J_p is photocurrent density, V_{app} is applied potential vs RHE, and I_0 is the irradiance intensity of 100 mW/cm² (AM 1.5G). The STH efficiency as a function of applied potential is plotted in Fig. 5c. Undoped TiO₂ NW, Sn/TiO₂ NW, and C/TiO₂ NW exhibit conversion efficiencies of 0.72%, 0.38%, and 0.32% at 0.55 V vs RHE respectively. Interestingly, the conversion efficiency for the (Sn, C) codoped TiO₂ NW photoanode is 1.32% at the same potential – representing 60%, 94%, and 100% efficiency improvements compared to the undoped, Sn doped, and C doped TiO₂ NW respectively. The improvements are attributed to efficient surface charge transfer by codoped TiO₂ NW as observed from the generation of high photocurrent densities at a lower applied bias. This might be due to improvements in surface properties e.g. surface trap

states by the synergetic effects of codopants. The photocurrent rises steeply starting from onset potentials up to 0.55 V vs RHE for the codoped sample, where it exhibited its maximum photoconversion efficiency. Improving the maximum photocurrent and reducing the photocurrent saturation and onset potentials substantially enhances the photoconversion efficiency of (Sn, C) codoped TiO₂ NW.

One thing we need to consider in photoelectrochemical investigations is the question of whether the recombination rate of photogenerated charge carriers is dependent on the applied potential [52,54]. At lower applied potentials charge carrier accumulation at the semiconductor/electrolyte interface takes place due to a high hole injection barrier. As a result, surface recombination between electrons and holes dominates the competing hole transfer to water oxidation. At high applied potentials the barrier no longer impedes hole transfer from the photoanode to the electrolyte, which means the hole that makes it to the interface participates in the oxidation of water. In this case, surface recombination is suppressed and hole transport from bulk to the interface limits the photocurrent [52]. Hence, for the codoped sample, we can see that the rate of hole transfer to the electrolyte with respect to the external applied bias reaches a maximum and surface recombination is suppressed at a minimum potential compared with the undoped and monodoped samples. This might be due to improved surface/interface

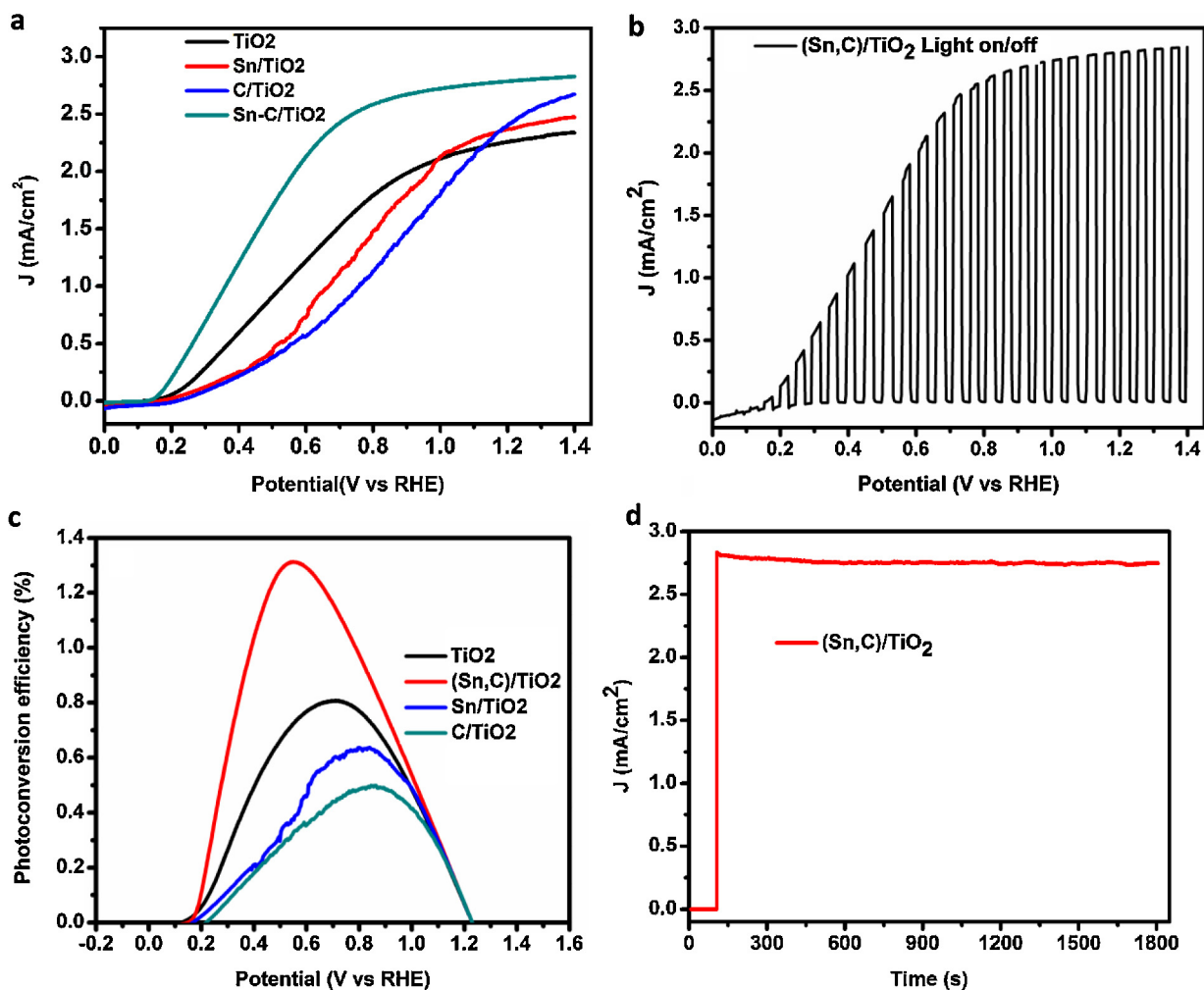


Fig. 5. (a) Photocurrent density as a function of applied potential, (b) photo/dark current density as a function of applied potential with on/off shutter for interrupting illumination, (c) corresponding photoconversion efficiencies for pristine, Sn only doped, C only doped, and (Sn, C) codoped TiO₂ NW as a function of applied potential, (d) photocurrent density–time profile obtained for the (Sn, C) codoped TiO₂ NW at 0 V vs. Ag/AgCl. All measurements were performed under 1 sun simulated light (AM1.5G, 100 mW/cm²) illumination.

properties for efficient hole transfer as a result of synergetic effects of codopants as well as defect formation like oxygen vacancy and Ti³⁺ during hydrogen treatment. Strong band bending due to large carrier density [55] can also have a positive effect in reducing charge recombination. The divergence of photocurrents at lower potentials and their convergence at higher potentials shows that the performance difference arises due to differences in the surface charge transfer rate. In monodoped samples, the dopants may act as surface recombination centers for photogenerated electrons and holes [56]. In a higher potential region where surface recombination no longer limits the photocurrent, the current of monodoped TiO₂ is higher than that for the undoped material.

The mechanism of photocurrent enhancement was also investigated using electrochemical impedance spectroscopy (EIS) measurements. This method is useful to give a semiquantitative comparison of samples that have similar morphology, material composition and device geometry [57]. The Mott–Schottky plots of pristine, codoped and monodoped samples are presented in Fig. 6. The plot for all the samples shows a positive slope as expected for n-type semiconductor. According to the Mott–Schottky equation [58],

$$\frac{1}{C^2} = \frac{2}{N_d e \epsilon_0 \epsilon} \left(E - E_{FB} - \frac{kT}{e} \right) \quad (2)$$

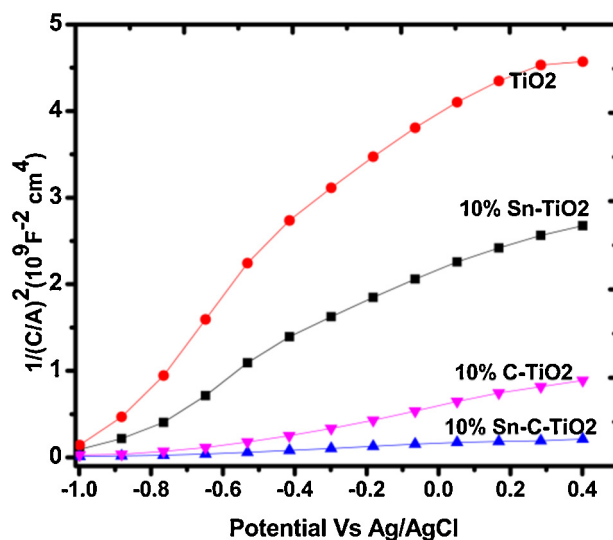


Fig. 6. The Mott–Schottky plot for pristine, codoped and monodoped TiO₂ NW photoanodes.

Table 1

Flat band potential (E_{FB}) and the charge carrier density (N_d) doped and pristine TiO₂ NWs.

Sample	E_{FB} (V) vs RHE	$N_d/10^{21} \text{ cm}^{-3}$	Sn at. %	C at. %
TiO ₂	−0.15	1.60	0	0
(Sn, C) doped TiO ₂	−0.06	5.93	3.2	7.4
Sn doped TiO ₂	−0.10	1.89	2.4	0
C doped TiO ₂	−0.13	2.30	0	5.6

where C is the space charge capacitance in the semiconductor, N_d is the charge carrier density, e is electron charge, ϵ_0 and ϵ are the vacuum permittivity and the relative permittivity of the semiconductor, respectively, E is the applied potential, E_{FB} is the flat band potential, T is the temperature, and k is the Boltzmann constant. The flat band potential value is estimated by extrapolating the Mott–Schottky plots to the x -axis (i.e., $1/C^2 = 0$) to get the intercept. The charge carrier density (N_d) can be calculated from the Mott–Schottky plots using the following equation [58].

$$N_d = \frac{2}{e\epsilon_0\epsilon} \left(\frac{dE}{d(1/C^2)} \right) \quad (3)$$

where the symbols are as noted in Eq. (2). For TiO₂ ($\epsilon = 170$) [59] the E_{FB} and N_d values are calculated and summarized in Table 1.

The flat band potential values correspond to the conduction band for n-type semiconductor photoelectrodes. The undoped TiO₂ NW has a more negative flat band potential. Introducing cations downshifts the conduction band to more positive values. The relatively positive flat band potential of (Sn, C) doped compared to the Sn only doped TiO₂ shows codoping to be a more effective way to modulate the conduction band edge and consequently band gap of TiO₂. This might be due to synergetic effects of the cation and anion increasing the amount of dopants introduced into the TiO₂ matrix as shown in XPS quantification results. Another reason for the difference in the performance of these materials is that the charge carrier density directly enhances the photocurrent density. It has a direct effect in enhancing the photocurrent density. In this regard, the codoped system has the highest charge carrier density as the Sn donor density and C acceptor density jointly contribute to enhancing the carrier density. In addition, the H₂ treatment increases donor density and electrical conductivity due to Ti³⁺ defect and charged oxygen vacancy formation in the material. The increased carrier density improves the charge transport as well as the electron transfer at the interface between the semiconductor and the FTO substrate. The C doped TiO₂ has also the next higher carrier density after the codoped TiO₂, while the photocurrent and STH efficiency is the lowest of all the samples. This might be due to large charge carrier recombination centers arising from unbalanced charged defects.

4. Conclusions

In summary, we fabricated a single crystal TiO₂ NW photoanode codoped with Sn and C, using a facile one pot hydrothermal method and investigated its PEC water Splitting comparison with monodoped and undoped TiO₂ NW arrays. From the XPS quantification results, the amounts of Sn and C in codoped system have been shown to be higher than in respective monodoped systems. This indicates the effect of codoping in improving the solubility limits of dopants. The (Sn, C) codoped TiO₂ NW photoanode generated a saturated photocurrent density of 2.8 mA/cm² at 1.23 V vs RHE and yielded a maximum solar energy conversion efficiency of 1.32% at a potential of 0.55 V vs RHE. This is 60%, 94%, and 100% efficiency improvement compared to undoped, Sn doped, and C doped TiO₂ NW respectively at same potential. To the best of our knowledge, this is currently the best report of photocurrent

density and solar energy conversion efficiency attained in PEC water splitting for a codoped TiO₂ NW photoanode. We attribute this to the synergetic effects of Sn and C: in reducing charge recombination at the surface, enhancing charge carrier density, improving light absorption and increasing the solubility limits of dopants (as evidenced by UV–vis spectroscopy, together with XPS, J – V and EIS measurements). The method described here shows the potential of codoping for improving the efficiency of TiO₂ for PEC water splitting by choosing appropriate cation–anion pairs.

Acknowledgements

The financial supports from the Ministry of Science and Technology (MoST) (103-3113-E-011-001, 101-3113-E-011-002, 101-2923-E-011-001-MY3, 100-2221-E-011-105-MY3), the Ministry of Economic Affairs (MOEA) (101-EC-17-A-08-S1-183), and the Top University Projects of Ministry of Education (MOE) (100H451401), as well as the facilities supports from the National Synchrotron Radiation Research Center (NSRRC) and National Taiwan University of Science and Technology (NTUST) are acknowledged. The authors also like to thank Mr. Liao (a staff member in materials science and engineering) for his support in TEM sample preparation using FIB (focused ion beam).

Appendix A. Supplementary data

Supplementary data associated with this article can be found, in the online version, at <http://dx.doi.org/10.1016/j.apcatb.2014.08.027>.

References

- [1] B.M. Klepser, B.M. Bartlett, *J. Am. Chem. Soc.* 136 (2014) 1694–1697.
- [2] J.R. McKone, A.P. Pieterick, H.B. Gray, N.S. Lewis, *J. Am. Chem. Soc.* 135 (2012) 223–231.
- [3] H. Yamashita, M. Harada, J. Misaka, M. Takeuchi, Y. Ichihashi, F. Goto, M. Ishida, T. Sasaki, M. Anpo, *J. Synchrotron Radiat.* 8 (2001) 569–571.
- [4] M. Wang, F. Ren, G. Cai, Y. Liu, S. Shen, L. Guo, *Nano Res.* 7 (2014) 353–364.
- [5] G. Wang, Y. Ling, D.A. Wheeler, K.E.N. George, K. Horsley, C. Heske, J.Z. Zhang, Y. Li, *Nano Lett.* 11 (2011) 3503–3509.
- [6] Y. Ling, G. Wang, D.A. Wheeler, J.Z. Zhang, Y. Li, *Nano Lett.* 11 (2011) 2119–2125.
- [7] G. Wang, Y. Ling, Y. Li, *Nanoscale* 4 (2012) 6682–6691.
- [8] A. Fujishima, K. Honda, *Nature* 238 (1972) 37.
- [9] J. Nowotny, C.C. Sorrell, T. Bak, L.R. Sheppard, *Sol. Energy* 78 (2005) 593–602.
- [10] M.R. Hoffmann, S.T. Martin, W. Choi, D.W. Bahnemann, *Chem. Rev.* 95 (1995) 69–96.
- [11] A.L. Linsebigler, G. Lu, J.T. Yates, *Chem. Rev.* 95 (1995) 735–758.
- [12] X. Chen, S.S. Mao, *Chem. Rev.* 107 (2007) 2891–2959.
- [13] M. Ni, M.K.H. Leung, D.Y.C. Leung, K. Sumathy, *Renew. Sustain. Energy Rev.* 11 (2007) 401–425.
- [14] T. Bak, J. Nowotny, M. Rekas, C.C. Sorrell, *Int. J. Hydrogen Energy* 27 (2002) 991–1022.
- [15] X. Liu, H. Zhang, X. Yao, T. An, P. Liu, Y. Wang, F. Peng, A. Carroll, H. Zhao, *Nano Res.* 5 (2012) 762–769.
- [16] Y. Yu, C. Cao, W. Li, P. Li, J. Qu, W. Song, *Nano Res.* 5 (2012) 434–442.
- [17] H. Tada, M. Fujishima, H. Kobayashi, *Chem. Soc. Rev.* 40 (2011) 4232–4243.
- [18] W. Choi, A. Termin, M.R. Hoffmann, *J. Phys. Chem.* 98 (1994) 13669–13679.
- [19] C. Das, P. Roy, M. Yang, H. Jha, P. Schmuki, *Nanoscale* 3 (2011) 3094–3096.
- [20] G. Wang, H. Wang, Y. Ling, Y. Tang, X. Yang, R.C. Fitzmorris, C. Wang, J.Z. Zhang, Y. Li, *Nano Lett.* 11 (2011) 3026–3033.
- [21] S.G. Kumar, L.G. Devi, *J. Phys. Chem. A* 115 (2011) 13211–13241.
- [22] R. Long, N.J. English, *Chem. Mater.* 22 (2010) 1616–1623.
- [23] W.-J. Yin, H. Tang, S.-H. Wei, M.M. Al-Jassim, J. Turner, Y. Yan, *Phys. Rev. B* 82 (2010) 045106.
- [24] Y. Gai, J. Li, S.-S. Li, J.-B. Xia, S.-H. Wei, *Phys. Rev. Lett.* 102 (2009) 036402.
- [25] P. Wang, Z. Liu, F. Lin, G. Zhou, J. Wu, W. Duan, B.-L. Gu, S.B. Zhang, *Phys. Rev. B* 82 (2010) 193103.
- [26] X. Ma, Y. Wu, Y. Lu, J. Xu, Y. Wang, Y. Zhu, *J. Phys. Chem. C* 115 (2011) 16963–16969.
- [27] B. Liu, E.S. Aydil, *J. Am. Chem. Soc.* 131 (2009) 3985–3990.
- [28] K. Shankar, J.I. Basham, N.K. Allam, O.K. Varghese, G.K. Mor, X. Feng, M. Paulose, J.A. Seabold, K.-S. Choi, C.A. Grimes, *J. Phys. Chem. C* 113 (2009) 6327–6359.
- [29] A. Wolcott, W.A. Smith, T.R. Kuykendall, Y. Zhao, J.Z. Zhang, *Small* 5 (2009) 104–111.
- [30] K. Vinodgopal, I. Bedja, P.V. Kamat, *Chem. Mater.* 8 (1996) 2180–2187.
- [31] M. Xu, P. Da, H. Wu, D. Zhao, G. Zheng, *Nano Lett.* 12 (2012) 1503–1508.

- [32] F. Sayilkan, M. Asiltürk, P. Tatar, N. Kiraz, Ş. Şener, E. Arpaç, H. Sayilkan, *Mater. Res. Bull.* 43 (2008) 127–134.
- [33] Y. Duan, N. Fu, Q. Liu, Y. Fang, X. Zhou, J. Zhang, Y. Lin, *J. Phys. Chem. C* 116 (2012) 8888–8893.
- [34] L. Xu, E.M.P. Steinmiller, S.E. Skrabalak, *J. Phys. Chem. C* 116 (2011) 871–877.
- [35] N. Siedl, S.O. Baumann, M.J. Elser, O. Diwald, *J. Phys. Chem. C* 116 (2012) 22967–22973.
- [36] J.H. Park, S. Kim, A.J. Bard, *Nano Lett.* 6 (2005) 24–28.
- [37] C. Di Valentin, G. Pacchioni, A. Selloni, *Chem. Mater.* 17 (2005) 6656–6665.
- [38] G. Wu, T. Nishikawa, B. Ohtani, A. Chen, *Chem. Mater.* 19 (2007) 4530–4537.
- [39] E.M. Neville, M.J. Mattle, D. Loughrey, B. Rajesh, M. Rahman, J.M.D. MacElroy, J.A. Sullivan, K.R. Thampi, *J. Phys. Chem. C* 116 (2012) 16511–16521.
- [40] E. Wang, T. He, L. Zhao, Y. Chen, Y. Cao, *J. Mater. Chem.* 21 (2011) 144–150.
- [41] C.H.L.S. Cho, Y. Feng, M. Logar, P.M. Rao, L. Cai, D.R. Kim, R. Sinclair, X. Zheng, *Nat. Commun.* 4 (2013) 1723.
- [42] J. Chen, L.B. Lin, F.Q. Jing, *J. Phys. Chem. Solids* 62 (2001) 1257–1262.
- [43] G. Li, L. Li, J. Boerio-Goates, B.F. Woodfield, *J. Am. Chem. Soc.* 127 (2005) 8659–8666.
- [44] C. Zhen, L. Wang, L. Liu, G. Q. Lu, H.-M. Cheng, *Chem. Commun.* 49 (2013) 6191–6193.
- [45] J. Tauc, *Mater. Res. Bull.* 3 (1968) 37–46.
- [46] X. Pan, M.-Q. Yang, X. Fu, N. Zhang, Y.-J. Xu, *Nanoscale* 5 (2013) 3601–3614.
- [47] X. Chen, L. Liu, P.Y. Yu, S.S. Mao, *Science* 331 (2011) 746–750.
- [48] E. Papirer, R. Lacroix, J.-B. Donnet, G. Nansé, P. Fioux, *Carbon* 33 (1995) 63–72.
- [49] S. Sakthivel, H. Kisch, *Angew. Chem. Int. Ed.* 42 (2003) 4908–4911.
- [50] Y. Park, W. Kim, H. Park, T. Tachikawa, T. Majima, W. Choi, *Appl. Catal. B: Environ.* 91 (2009) 355–361.
- [51] Y. Li, D.-S. Hwang, N.H. Lee, S.-J. Kim, *Chem. Phys. Lett.* 404 (2005) 25–29.
- [52] H. Dotan, K. Sivula, M. Gratzel, A. Rothschild, S.C. Warren, *Energy Environ. Sci.* 4 (2011) 958–964.
- [53] B. Parkinson, *Acc. Chem. Res.* 17 (1984) 431–437.
- [54] Z. Chen, T.F. Jaramillo, T.G. Deutsch, A. Kleiman-Shwarscstein, A.J. Forman, N. Gaillard, R. Garland, K. Takanabe, C. Heske, M. Sunkara, E.W. McFarland, K. Domen, E.L. Miller, J.A. Turner, H.N. Dinh, *J. Mater. Res.* 25 (2010) 3–16.
- [55] Z. Zhang, J.T. Yates, *Chem. Rev.* 112 (2012) 5520–5551.
- [56] K. Maeda, *J. Photochem. Photobiol. C: Photochem. Rev.* 12 (2011) 237–268.
- [57] Y. Wang, Y.-Y. Zhang, J. Tang, H. Wu, M. Xu, Z. Peng, X.-G. Gong, G. Zheng, *ACS Nano* 7 (2013) 9375–9383.
- [58] M. Ye, J. Gong, Y. Lai, C. Lin, Z. Lin, *J. Am. Chem. Soc.* 134 (2012) 15720–15723.
- [59] R.A. Parker, *Psychol. Res.* 124 (1961) 1719–1722.